ADVANCED MATERIALS
www.advmat.de

Stable Sodium-Metal Batteries in Carbonate Electrolytes Achieved by Bifunctional, Sustainable Separators with Tailored Alignment

Jing Wang, Zhen Xu, Qicheng Zhang, Xin Song, Xuekun Lu, Zhenyu Zhang, Amaka J. Onyianta, Mengnan Wang, Maria-Magdalena Titirici, and Stephen J. Eichhorn**

Sodium (Na) is the most appealing alternative to lithium as an anode material for cost-effective, high-energy-density energy-storage systems by virtue of its high theoretical capacity and abundance as a resource. However, the uncontrolled growth of Na dendrites and the limited cell cycle life impede the large-scale practical implementation of Na-metal batteries (SMBs) in commonly used and low-cost carbonate electrolytes. Herein, the employment of a novel bifunctional electrospun nanofibrous separator comprising well-ordered, uniaxially aligned arrays, and abundant sodiophilic functional groups is presented for SMBs. By tailoring the alignment degree, this unique separator integrates with the merits of serving as highly aligned ion-redistributors to self-orientate/homogenize the flux of Na-ions from a chemical molecule level and physically suppressing Na dendrite puncture at a mechanical structure level. Remarkably, unprecedented long-term cycling performances at high current densities (≥1000 h at 1 and 3 mA cm^{-2}, ≥700 h at 5 mA cm^{-2}) of symmetric cells are achieved in additive-free carbonate electrolytes. Moreover, the corresponding sodium–organic battery demonstrates a high energy density and prolonged cyclability over 1000 cycles. This work opens up a new and facile avenue for the development of stable, low-cost, and safe-credible SMBs, which could be readily extended to other alkali-metal batteries.

1. Introduction

The rapid advancements in emerging portable electronics, transportation (e.g., electric vehicles, hybrid electric vehicles, autonomous aircraft, etc.), and smart grid-scale energy storage have stimulated the ever-growing demand for high-energy-density, highly safe, and low-cost energy-storage systems.[1–4] Nevertheless, the continuous large-scale application of lithium-ion batteries (LIBs) is constrained by their soaring cost, considering the shortage and uneven distribution of lithium resources, which is often also associated with poor environmental and human rights records, prompting the replacement of conventional LIBs with new battery systems.[5–7] Among numerous anode materials, sodium (Na) metal is regarded as a promising anode for next-generation of rechargeable batteries due to its high theoretical specific capacity (1165 mAh g^{-1}), low redox potential (−2.714 V versus standard hydrogen

J. Wang, Q. Zhang, A. J. Onyianta, S. J. Eichhorn
Bristol Composites Institute
School of Civil, Aerospace, and Mechanical Engineering
University of Bristol
University Walk, Bristol BS8 1TR, UK
E-mail: jw17476@bristol.ac.uk; s.j.eichhorn@bristol.ac.uk
Z. Xu
Yusuf Hamied Department of Chemistry
University of Cambridge
Cambridge CB2 1EW, UK
The ORCID identification number(s) for the author(s) of this article can be found under https://doi.org/10.1002/adma.202206367.

DOI: 10.1002/adma.202206367

X. Song
Department of Materials
Department of Bioengineering and Institute of Biomedical Engineering
Imperial College London
Prince Consort Road, London SW7 2AZ, UK
X. Lu, Z. Zhang
Electrochemical Innovation Lab
Department of Chemical Engineering
University College London
Torrington Place, London WC1E 7JE, UK
X. Lu
School of Engineering and Materials Science
Queen Mary University of London
Mile End Rd, London E1 4NS, UK
M. Wang, M.-M. Titirici
Department of Chemical Engineering
Imperial College London
South Kensington Campus
London SW7 2AZ, UK

electrode), and abundant resources (Na with 2.83 wt% in the Earth's crust and Li with 0.0017 wt%).[8,9] Rechargeable sodium-metal batteries (SMBs) based on Na-metal anodes and high-voltage intercalation cathodes[10] or energetic conversion cathodes (e.g., Na–O_2, Na–CO_2, Na–SO_2, room temperature Na–S or Na–$CuCl_2$),[11–15] have gained considerable attention owing to their low cost and ultrahigh theoretical energy densities (e.g., 1125 Wh kg^{-1} for Na–CO_2, and 1605 Wh kg^{-1} for Na–O_2 batteries with the formation of Na_2O_2), which hold great promise as an extremely appealing alternative to today's state-of-the-art LIBs.[16,17]

In contrast with LIBs and sodium-ion batteries which correspond to the insertion of Li^+/Na^+ into carbonaceous anode materials, SMBs possess the identical "plating/stripping" principle where the sodium ions are transformed into solid sodium metal and deposited on the sodium anode surface via a surface redox reaction.[18] However, the high reactivity with liquid electrolytes and substantial volume change of the Na-metal anode, combined with an unstable solid electrolyte interphase (SEI) induces a nonuniform Na plating with Na dendritic growth upon cycling, which can bring about a low Coulombic efficiency (CE), limited cyclability and even safety hazards.[19,20] Notably, the uncontrolled Na dendrite growth during repetitive stripping/platting can penetrate through the separator to reach the cathode and cause an internal short circuit in rechargeable battery systems, ultimately resulting in catastrophic thermal runaway, fire, and even explosion.[21] Numerous strategies have been employed to circumvent these shortcomings and safety issues of SMBs, including formulating electrolyte systems (e.g., ultraconcentrated electrolyte, fluoroethylene carbonate additives),[22,23] constructing artificial SEI layers (e.g., NaBr, graphene/Na, Al_2O_3),[24–26] designing solid-state/gel polymer electrolytes (e.g., $Na_3Zr_2Si_2PO_{12}$, graphene oxide/polyvinylidene fluoride-hexafluoropropylene),[27,28] and applying nanostructured Na anodes (e.g., porous Al, N/S-doped carbon nanotubes (CNTs) paper, reduced graphene oxide).[29–31] Nevertheless, these kinds of design schemes mainly focus on optimizing the electrolyte systems and the Na-metal anodes to improve the electrochemical stability at the expense of high viscosity, expensive salt costs, large interfacial resistance and thickness, low ionic conductivity, and tedious synthesis procedures, which still pose the remaining issues associated with the widespread commercialization of SMBs.[32,33]

As an important component of cells, separators act as a pivotal role in preventing the electronic contact of cathodes/anodes but also allow the transmission of ions between electrodes, which can determine the cell's electrochemical performance.[34,35] Recently, it has been reported that high-modulus separators for SMBs, such as solid-state electrolyte (SSE) membranes, can function as a mechanical barrier to block the Na dendrite growth while suffering from the relatively low ionic conductivity and unfavored interfacial compatibility between the electrode and SSE.[36,37] On the other hand, a few investigations have demonstrated that the utilization of "sodiophilic" interlayers with abundant polar functional groups can homogenize Na-ion flux on the anode surface with the lack of sufficient mechanical strength to withstand the tremendous volume change of Na-metal anodes.[38,39] Additionally, several recent reports mentioned the introduction of ion redistributor phases on the separator such as nanoporous SiO_2 nanosheets, or mesoporous cellulose nanofibers, for uniformly redistributing the ion flux or channeling the electrolyte via the pores/interspaces within functional coatings;[40] however, the additional weight/volume and cost introduced by the functional interlayers or phase would cause the extra electrolytes required for full wetting and reduce the cell-level energy density. More importantly, the long-term stable plating/stripping (e.g., ≥1000 h) of Na anodes in carbonate-based electrolytes even under limited current densities (mostly no more than 1 mAh cm^{-2}) still remains challenging; carbonate-based electrolytes show lower volatility and a wider electrochemical window, which can be coupled with high-potential cathodes in the pursuance of high-energy SMBs.[41]

Accordingly, it is imperative to fabricate advanced separators that simultaneously possess favorable mechanical strength, valuable sodiophilic features, and high wettability (i.e., uniformly homogenize Na-ion flux and suppress the dendritic Na growth) in carbonate-based electrolytes to boost the performance of Na-metal anodes under high current densities. Equally importantly, materials sustainability is an overriding factor, considering the economic and environmental benefits for large-scale practical production. As a prime alternative to costly and non-biodegradable materials (e.g., CNTs and graphene), cellulose nanocrystals (CNCs) are potentially biodegradable and are structural nanomaterials with the additional merits of large-scale availability at a relatively low cost, conjointly with being extracted from the most abundant resource (i.e., cellulose) and possessing high tensile moduli in the range of 110–220 GPa.[42,43] Notably, when the CNCs are extracted from the waste cellulose fraction of alginate production from brown seaweed, that otherwise would have gone into landfills, it exemplifies a circular and sustainable system of turning a ubiquitous biomass or waste into high-value products.[44]

In this work, we innovatively develop bi-functional, mechanically flexible, and low-cost brown-seaweed-derived CNC/polyetherimide (PEI) electrospun nanofibrous separators with desirable merits for the large-scale applications of inexpensive, safe-credible, and high-energy SMBs (see **Figure 1**). Our material design integrates the following advantages: i) regulating the Na-ion flux and the nucleation behavior to homogenize Na electrodeposition on the anode surface; ii) mechanically blocking the Na dendrite growth or puncture of Na dendrites to inhibit the short circuit; iii) readily tailoring the alignment and thickness of high-thermal-stability separators, paired with renewable organic electrodes to promote the total safety and sustainability of a cell configuration. It is noteworthy that most of the long-term stable SMBs are evaluated in ether-based electrolytes; there are few reports on the long cycle life of SMBs in carbonate-based electrolytes. These electrolytes are regarded as the commonly used choice for commercial LIBs, which possess many merits, including their low cost, better oxidation stability, and higher reduction potential that allows for high-voltage cathode materials.[45] To the best of our knowledge, this is the very first and highly desired report on achieving stable and long-term cycling stability under high current densities (i.e., ≥1000 h at 1 and 3 mA cm^{-2}, ≥700 h at 5 mA cm^{-2}) of SMBs operated in carbonate electrolytes without any additives.

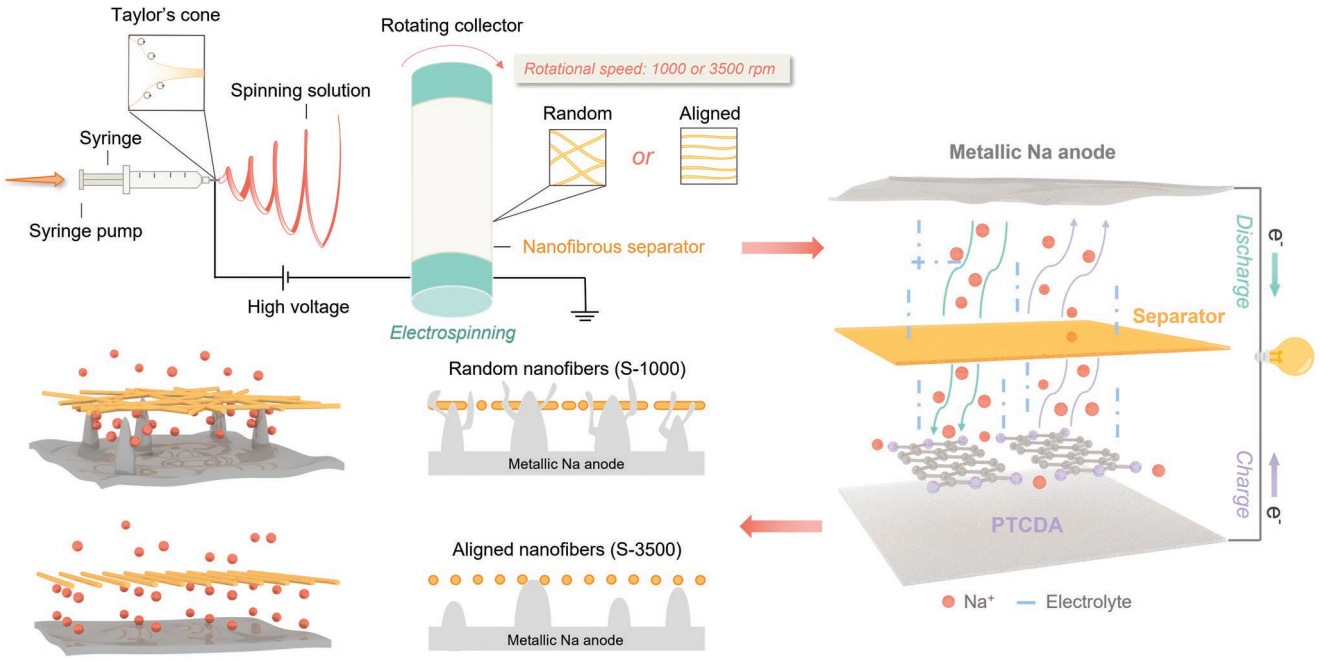

Figure 1. Schematic of the fabrication of electrospun CNC/PEI nanofibrous membranes and Na deposition behaviors with S-1000 and S-3500 separators for Na-metal batteries (PTCDA: 3,4,9,10-perylene-tetracarboxylicacid-dianhydride).

2. Results and Discussion

Figure 1 illustrates the synthesis process and Na deposition behavior of electrospun CNC/PEI hybrid nanofibrous separators for SMBs. First, a liquid droplet of a CNC/PEI spinning solution from the spinneret is deformed into a Taylor cone upon the application of a high-voltage electric field, from which the charged jet is ejected and stretched into finer diameters deposited on the grounded rotating drum collector following solidification. By adjusting the rotational speed of the rotating drum collector, oriented fiber arrays with a controllable degree of uniaxial alignment can be achieved.[46–48] Meanwhile, nanofibrous membranes with less-aligned or randomly oriented nanofibers (denoted as S-1000) were obtained using a relatively low rotational speed of 1000 rpm. The high rotational speed (3500 rpm) of the rotating drum collector induces a uniaxial alignment of the nanofibers, resulting in well-aligned nanofibrous separators (referred to as S-3500). Finally, the as-made sustainable, electrospun CNC-based nanocomposite nanofibrous separators (i.e., S-1000 and S-3500) with well-defined thickness and areal weight (A_W) were employed for SMBs. It is worth noting that this unique electrospinning strategy can effectively realize the strong coupling of the sodiophilic functional groups of CNCs and PEI, as well as well-ordered uniaxially aligned nanofibers with a tailored degree of alignment. These features are highly beneficial for constructing multifunctional ion-redistributors to homogenize Na-ion deposition for dendrite-oriented Na-metal anodes, as confirmed by the following results and analysis.

The as-fabricated CNC/PEI nanocomposite nanofibrous separators show no conspicuous damage when subjected to random folding, twisting, or rolling under various bending conditions as shown in **Figure 2**a; this demonstrates the prerequisites of good mechanical flexibility for separators in batteries. Figure S2, Supporting Information presents a typical transmission electron microscopy (TEM) image of the prepared *Laminaria hyperborea* seaweed-derived CNCs which are rod-shaped, high-crystalline nanocrystals with a high aspect ratio of 12–35 (160–210 nm in length; 6–12 nm in width) as a renewable nano-reinforcement phase of CNC/PEI nanocomposite fiber membranes. The electrolyte wettability of well-aligned CNC/PEI nanocomposite nanofibrous separators, commercial Celgard-2500 separator, and glass microfiber filters membrane (Grade GF/D, Whatman) was evaluated by contact angle measurements in the electrolytes (i.e., 1.0 M $NaClO_4$ in 1:1 (v/v) ethylene carbonate/dimethyl carbonate), where the contact angle of electrolyte on commercial Celgard separator is ≈26° (Figure 2b). Notably, the S-3500 and GF/D separators exhibit superior electrolyte wettability with a contact angle of close to zero, indicating an enhanced affinity of S-3500 with the carbonate-based electrolyte that is likely conducive to Na-ion diffusion.[49] The microstructures of the electrospun CNC/PEI composites nanofibers were first revealed in 3D reconstructions from X-ray computed tomography (Figure 2c,d), presenting their varied uniaxial alignment degree by regulating the rotational speeds (1000, 3500 rpm) of the rotating collector. It is noted from Figure 2c that the scanning electron microscopy (SEM) image from the top view exhibits relatively randomly oriented nanofibers in the S-1000 nanofibrous membranes with several defects such as beads. Conversely, the nanofibers in the S-3500 nanofibrous mat became uniaxially aligned arrays with the improved orders and fewer defects from its top-view SEM image, which is consistent with the corresponding 3D computed tomography reconstructions (see Figure 2d). The increase in the rotating speed leads to the average fiber diameter decreasing to ≈550 nm (S-3500) from ≈760 nm (S-1000). This can be attributed to the enhanced extensional forces from

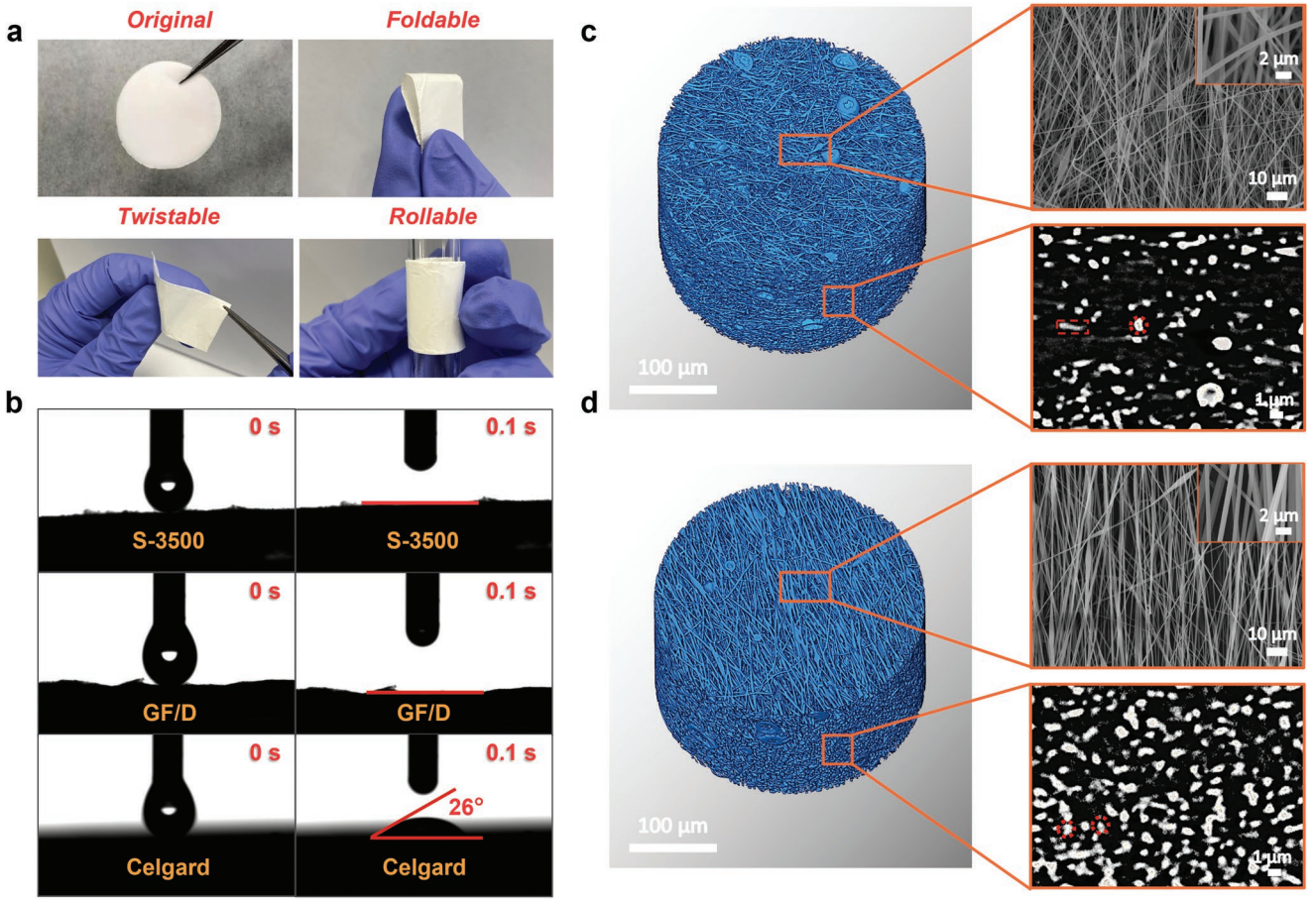

Figure 2. Structural properties and microstructures of separators. a) Folding, twisting, and rolling tests for CNC/PEI nanocomposite nanofibrous separators. b) Contact angles of the electrolyte on S-3500, GF/D, and Celgard separators. c,d) 3D reconstructions (left), typical SEM images from the top view (top) and cross-sectional representation (bottom) derived from X-ray microtomography of S-1000 (c) and S-3500 (d) nanofibrous separators. The insets are the magnified top-view SEM images.

the higher speed of the drum collector rotation, causing the jet to be drawn into thinner nanofibers with a greater degree when being ejected away from the spinneret.[50] Furthermore, it is observed from the 2D representation of cross-sectional X-ray tomography that the S-3500 hybrid mat shows a uniform and smaller tubular architecture perpendicular to the nanofiber orientation with a higher homogeneity throughout the mat, in contrast to the S-1000 that has an irregular and a larger cylindrical nanostructure with more voids (red dashed rectangle denotes a cross-sectional morphology of nanofibers in Figure 2c,d). Based on these observations, we conclude that the higher rotation speed of the drum collector results in smaller and finer nanofibers as well as more uniaxially aligned and bead-free arrays over large areas.

Fourier-transform infrared (FT-IR) spectra of the hybrid CNCs/PEI nanofibrous membranes reveal the existence of the characteristic bands of CNCs at ≈2900 and 1034 cm^{-1} assigned to C—H bonds stretching and hydroxyl (C—OH) groups at the C_6 position of cellulose structure, and the characteristic vibration bands located at ≈1720 and 1355 cm^{-1} corresponding to carbonyl (C=O) groups and the C—N stretch of PEI (**Figure 3**a).[51] This demonstrates the physical hybridization of CNCs and PEI without chemical reaction in the as-prepared nanofibrous separators (i.e., S-1000 and S-3500) during the electrospinning process. Furthermore, it is evidenced that the abundant polar functional groups (e.g., C=O, —OH) are present in S-1000 and S-3500 hybrid nanofibrous separators, favoring sodiophilic properties and superior electrolyte wettability at the molecular level.[52] According to electrochemical impedance spectroscopy (EIS) plots (Figure 3b), the symmetric stainless steel‖stainless steel cells with S-3500 separators exhibit a much lower bulk resistance (R_b) of 4.3 Ω in comparison with those of S-1000 (24.0 Ω), GF/D (29.6 Ω) and Celgard (37.5 Ω); the corresponding calculated ionic conductivity (σ_i) according to Equation S2, Supporting Information was also presented (Figure 3g). Besides, the Na^+ transference number (t_{Na^+}) of various separators is shown in Figure S3, Supporting Information using Equation S3, Supporting Information; it displays a high t_{Na^+} of 0.83 compared with the conventional Celgard material of only 0.41 (Table S1, Supporting Information). This enhancement may be ascribed to the sodiophilic functional groups stemming from the S-3500 separator to promote the transport of cations. Hence, the improved ionic conductivity and transference number of cations in the symmetric cell with an S-3500 separator would suggest the highest transport kinetics and help to suppress dendrites formation during the Na plating/stripping process based on the

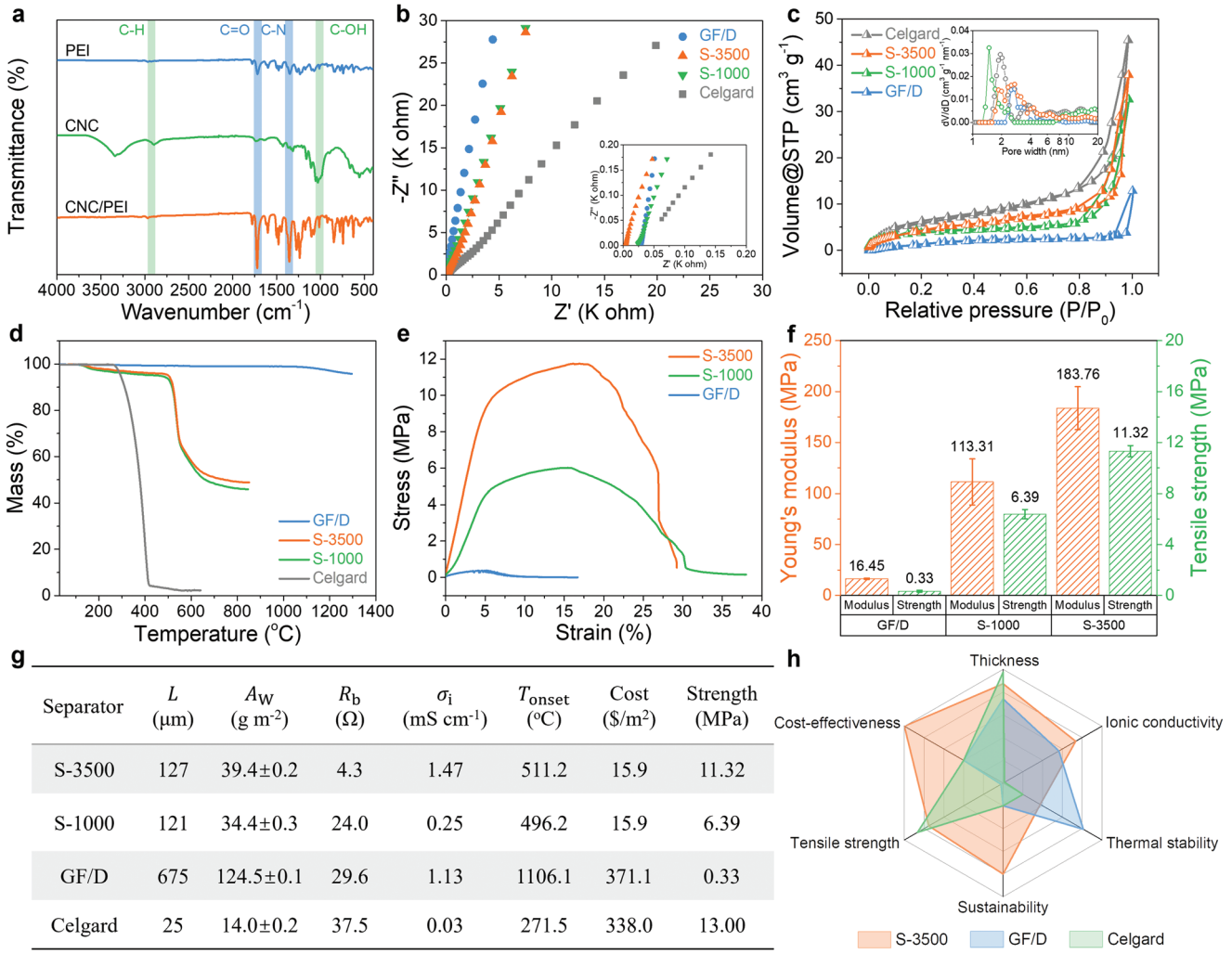

Separator	L (μm)	A_W (g m^{-2})	R_b (Ω)	σ_i (mS cm^{-1})	T_{onset} (°C)	Cost ($/m^2)	Strength (MPa)
S-3500	127	39.4±0.2	4.3	1.47	511.2	15.9	11.32
S-1000	121	34.4±0.3	24.0	0.25	496.2	15.9	6.39
GF/D	675	124.5±0.1	29.6	1.13	1106.1	371.1	0.33
Celgard	25	14.0±0.2	37.5	0.03	271.5	338.0	13.00

Figure 3. Evaluation of physiochemical parameters for SMB separators. a) FT-IR spectrum of the CNC/PEI hybrid nanofibrous membranes. b) EIS analysis, c) nitrogen adsorption-desorption isotherms and pore-size distributions (inset), d) TGA thermograms, e) stress–strain curves, f) tensile mechanical properties (Young's modulus, strength), g) summary of physical and chemical parameters, and h) radar charts of key properties indicators for S-1000, S-3500, GF/D and Celgard separators. The vital parameters are ranked on a scale from 1 to 5; particularly, a smaller thickness ranks as a higher value.

space-charge theory,[53] possibly owing to the favorable oriented ion-flux pathways originating from well-ordered uniaxial aligned arrays/nanofibers.[54] Moreover, typical type IV N_2 adsorption/desorption isotherms with H2-type hysteresis loops and pore size distribution curves confirm the porosity of our hybrid nanofibrous separators (Figure 3c,g). According to the *n*-butanol uptake tests, the S-3500 separator shows a well-developed porous structure (e.g., parallel nanofibers gaps between well-oriented nanofibers and micro/mesopores within nanofibers) and a favorable porosity (P) of 58.9% (see Equation S5, Supporting Information) that ensures a sufficient electrolyte inclusion to facilitate fast pathways for Na ionic diffusion and hence minimize the internal resistance;[55] the relatively higher Brunauer–Emmett–Teller (BET) specific surface area (S_{BET}) was obtained for these materials compared with those of S-1000 and GF/D (see Table S1, Supporting Information).

Notably, the safety characteristics of the separator are critical parameters to evaluate in terms of the separator's resistance to deformation from thermal abuse (thermal runaway) and mechanical abuse (crush and penetration, etc.).[56,57] Specifically, the thermal stability of the separators correlated with their shrinkage at elevated temperatures and ultimate internal short-circuit, is one safety characteristic regarding the realization of stable and high-safe SMBs with a practical and extended operating temperature range. Thermogravimetric analysis (TGA) curves in Figure 3d illustrate that the Celgard-2500 separator experienced a drastic weight loss of over 95% from 280 to 410 °C resulting from the degradation of polypropylene (PP), whereas the CNC/PEI composite separators (i.e., S-1000, S-3500) exhibited a negligible weight loss of ≈2% in the same temperature range with a synchronous first-step thermal decomposition process of CNCs with T_{onset} at ≈278 °C.[58] Interestingly, the decomposition temperatures of the PEI matrix for S-1000 and S-3500 separators were ≈512 and ≈516 °C, respectively, signifying a small enhancement of the thermal stability with an increased uniaxial alignment degree or rotational speed of the

drum collector. GF/D separators presented no pronounced weight loss before 1100 °C due to their constitution as a thermally resistant borosilicate glass (SiO_2, B_2O_3) microfiber-based filter.[59] Figure 3e shows representative stress–strain curves for commercial separators and our CNC/PEI nanofibrous membranes. The S-1000 nanofibrous mat with a relatively random fiber array has a tensile strength of 6.4 ± 0.4 MPa, while the value is increased by 76.7% to 11.3 ± 0.4 MPa (≈13 MPa for the Celgard membrane).[60] The uniaxially aligned S-3500 mat yields a higher Young's modulus of 183.8 ± 21.0 MPa, signifying its mechanically-stiff nature (see Figure 3f). By comparison, commercial GF/D separators possess much lower mechanical properties: their tensile strength and Young's modulus are only 0.3 ± 0.1 and 16.4 ± 0.6 MPa, respectively. Accordingly, compared with GF/D and S-1000 separators, our S-3500 membrane manifests superior mechanical properties to meet the practical requirements on account of the presence of the strong and stiff CNCs as reinforcing nano-fillers and the highly uniaxial alignment of the CNC/PEI nanofibers. Overall, the highly aligned hybrid nanofibrous separators, made with a simple and scalable fabrication procedure, provide a superior wettability and ionic conductivity, exceptional mechanical strength, together with the optimum thickness and thermal stability for safe-credible SMBs. Comparison of key performance indicators suggests that sustainable, low-cost, mechanically flexible nanofibrous membranes (i.e., S-1000, S-3500) are promising and prospective alternatives to the benchmark Celgard materials or GF/D membranes (Figure 3h, the key parameters for this ranking were given in Figure 3g and Table S1, Supporting Information).

Considering the aforementioned physiochemical merits of the CNC/PEI nanofibrous separators, the overall electrochemical performance of symmetric Na||Na cells with the S-1000, S-3500, and GF/D counterparts is further investigated using an electrolyte of 1.0 M $NaClO_4$ in ethylene carbonate/dimethyl carbonate (EC: DMC = 1:1, v/v) solution. It is worth noting that the utilization of carbonate-based electrolytes in Na-metal batteries is an enormous challenge, owing to the formation of an unstable SEI layer and relatively positive reduction potential.[61,62] Therefore, the investigation of the applicable separators in a carbonate environment is significantly meaningful; particularly, commercial Celgard separators are inappropriate for highly safe, high-temperature, and high-rate SMBs due to their unsatisfactory thermal stability and inferior wettability with carbonate-based electrolytes. It is noteworthy that Na||Na symmetric cells with a Celgard-2500 separator lead to premature short-circuits in the initial two cycles at 1 mA cm^{-2} and 0.5 mAh cm^{-2}; hence, the Celgard separator was not included in the subsequent comparisons regarding electrochemical performances for half/full cells and ex situ characterization for cycled cells. **Figure 4**a presents the voltage–time profiles of Na||Na cells with S-1000, S-3500, and GF/D separators at 1 mA cm^{-2}, 0.5 mAh cm^{-2}. Notably, the cells with the S-3500 highly aligned nanofibrous separator deliver flat voltage plateaus over 1000 h, illustrating their excellent cycling stability and good interfacial stability. In sharp contrast, the cells with the S-1000 relatively random separator display a gradual increase in voltage hysteresis after 200 h, ultimately micro-short circuiting at 330 h; an abrupt short circuit is observed for the cell with the GF/D separator after cycling for only 100 h, which can be ascribed to the puncture of growing Na dendrites through the GF/D separator due to its low mechanical resistance. Additionally, the rate voltage profiles of symmetric Na||Na cells are compared in Figure 4b for the nanofibrous separators (i.e., S-1000 and S-3500) and Figure S4, Supporting Information for the GF/D separator. The cells with the S-3500 separator show a stable and small overpotential when increasing current densities from 0.1 to 2 mA cm^{-2}, whereas the cells using the S-1000 separator suffer from a larger potential hysteresis and fluctuation at a current density of up to 2 mA cm^{-2}, implying the uncontrolled formation of sodium dendrites. These results demonstrate that the uniaxial aligned nanofibers/arrays in S-3500 separators are advantageous to regulate Na deposition and suppress dendrite growth at different current densities, giving rise to enhanced rate capabilities.

When the current density is increased to 3 mA cm^{-2}, the symmetric cells with the unique S-3500 separator still exhibit excellent long-term cycling stability with a small stripping/plating overpotential for over 1000 h, greatly outperforming the cells with the GF/D separator (Figure 4c). Only a slight increase in potential hysteresis for the cells with the S-3500 separator is observed in the 990th–1000th cycles compared with those in the fourth to sixth cycles (see insets in Figure 4c). When the stripping/plating capacity is substantially increased to 2.5 mAh cm^{-2}, which approaches that of current commercial high-energy batteries (<4 mAh cm^{-2}),[63] near stable Na plating/stripping over 700 h can still be retained for the cell with the S-3500 separator even at a very high current density of 5 mA cm^{-2}, whereas the cell with the GF/D separator can only be stably cycled for less than 7 h, and is ultimately terminated by an unexpected breakdown of the coin cell in operation (Figure 4e and Figure S5, Supporting Information). The significant differences in cycling performance strongly prove the superiority of the S-3500 separator in repeated plating and stripping processes of Na. In an ether-based electrolyte (i.e., 1.0 M NaPF6 in diglyme), the cycling stability of cells with the S-3500 separator again performs stable plating/stripping potential plateaus over 1000 h at a current density of 1 mA cm^{-2}, implying its potential employment promises in wide-ranging electrolytes for Na-metal batteries (see Figure S6, Supporting Information). To the best of our knowledge, such a long cycle life of cells assembled with our S-3500 separator (>1000 h at 1 mA cm^{-2}, >1000 h at 3 mA cm^{-2}, and >700 h at 5 mA cm^{-2}) surpasses those of all previously reported Na-metal batteries stabilized by various strategies employed in carbonate-based electrolytes, such as using a sodium benzenedithiolate (PhS_2Na_2) protection layer (800 h at 1 mA cm^{-2}),[39] Na@3D-$Na_3V_2(PO4)_3$ (NVP) electrode (400 h at 2 mA cm^{-2}) with 5 wt% fluoroethylene carbonate (FEC) electrolyte additives,[64] the Celgard-2400 separator coated with the Li-ion activated tin sulfide graphene (A-SnS-G) layer (500 h at 4 mA cm^{-2}) combined with 5% FEC electrolyte additives,[65] Na/In/C composite anode (560 h at 5 mA cm^{-2}) with 5 wt% FEC,[66] as shown in Figure 4f and Table S2, Supporting Information.[67–69] Remarkably, such an ultrahigh cumulative capacity of 3500 mAh cm^{-2} (current density × cycle life)[70] at a high-rate current density (5 mA cm^{-2}, 2.5 mAh cm^{-2}) is achieved in a commonly used carbonate-based electrolyte system without any additives, revealing the great superiority of our high-aligned nanofibrous separator (S-3500) design for

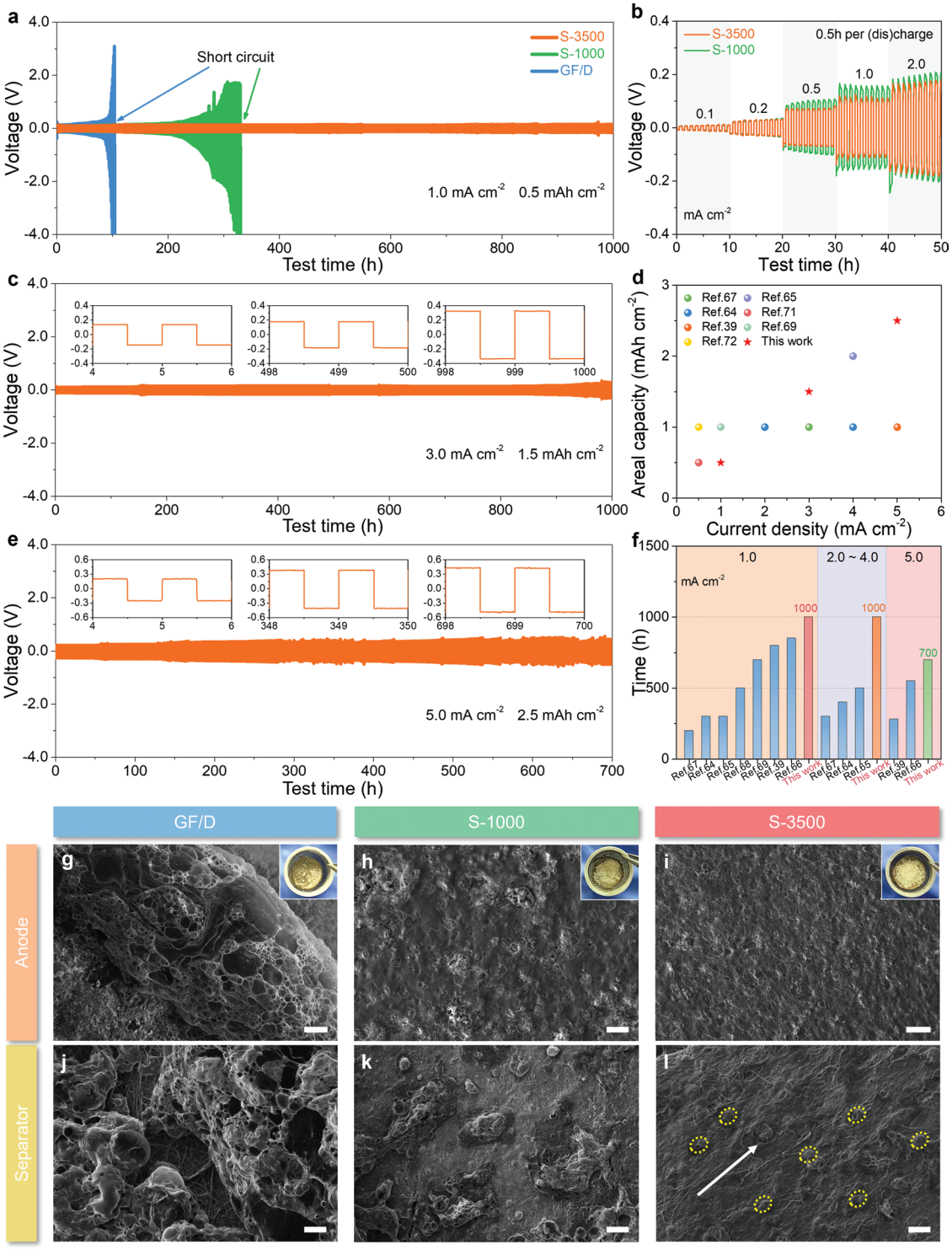

Figure 4. Electrochemical performances of Na||Na symmetric cells with various separators. a) Voltage–time profiles of Na plating/stripping processes at 1 mA cm^{-2}, 0.5 mAh cm^{-2}, and b) rate performance of Na||Na cells with GF/D, S-1000, and S-3500 separators at different current densities. c,e) Voltage–time profiles of Na||Na cells with S-3500 separator at current densities of 3 mA cm^{-2} (c), and 5 mA cm^{-2} (e) (insets: magnified voltage profiles at initial, intermediate, and final stage). d,f) Comparison of Na||Na cells with S-3500 separator and other previously reported works regarding rate performance (d) and cycling stability (f) obtained at various current densities employed in carbonate-based electrolytes. g–l) Ex situ SEM images of the anode side (g–i) and the separator side (j–l) for cycled Na||Na cells assembled with GF/D (g,j), S-1000 (h,k), and S-3500 (i,l) separators after 30 cycles at 1 mA cm^{-2}; the insets show digital photographs of the cycled Na-metal anodes in the coin cells. The uniaxial alignment of nanofibers is indicated by white arrows. Scale bars: g–l 100 µm.

SMBs with outstanding stability and cyclability at a wide range of current densities and plating/stripping capacities based on Figure 4d and Table S3, Supporting Information.[71,72]

To visually shed light on the effect of the S-3500 separator on the Na plating/stripping process, the morphologies of Na-metal anodes and separators stemming from cycled symmetric cells are investigated and traced by ex situ SEM (Figure 4g–l). Figure 4g–i presents the SEM images of the cycled anodes assembled with the GF/D, S-1000, and S-3500 separators after repeated plating/stripping cycles for 30 h in the plated condition. As shown in Figure 4g,h, 3D large-surface-area and moss-like Na dendrites are very pronounced on the Na foil surface for cells with a GF/D separator, while cells with a S-1000 separator display a rough surface with relatively smaller amounts of dendritic Na. Prominently, the S-3500 separator endows the plated Na foil with a rather smooth and flat surface morphology without any obvious dendrite growth after 30 cycles, which suggests a more homogenous electrodeposition/stripping procedure with a lower deposition overpotential; the content of moss-like Na dendrites is closely correlated with the increased overpotential during repeated cycles.[37] Meanwhile, SEM top-down images of the separator side for cycled cells with all three separators after 30 cycles were provided to further visualize their morphological evolution during the Na plating/stripping process (Figure 4j–l). The cycled GF/D separator side displays loosely stacked moss-like Na dendrites with a porous structure after 30 cycles, whereas small and large dendrites are detected on the cycled S-1000 separator side (Figure 4j,k). Surprisingly, the cycled S-3500 separator side reveals well-oriented minimal spherical dendrites (denoted by yellow dashed circles) parallel to the nanofiber's alignment on the S-3500 nanofibrous membrane (see Figure 4l), in which Na ions are homogenously distributed by the highly aligned nanofibers with sodiophilic functional groups. Intuitively, the insets of Figure 4g–i exhibit the digital photographs of mossy Na electrodeposits on the post-30 cycled Na foil surface in the fully plated state. The Na foil surface is dim and coarse in coin cells with GF/D separators due to the excessive consumption of electrolytes by reacting with the exposed large-surface-area and porous Na dendrites;[72] conversely, the bright and compact Na foil surface reveals the suppression of Na dendrite growth under identical conditions when the S-3500 separator is used (see the magnified pictures in Figure S7, Supporting Information). Such a completely distinctive appearance in the surface morphology of the cycled Na anode and separator side highlights the merits of the unique S-3500 separator comprising highly- aligned arrays with a sodiophilic nature to build smooth Na electrodeposition on both the anode and separator; this is in good agreement with the superior results of the corresponding Na||Na cells among all three separators at high current densities and large cycling capacities in Figure 3a–f.

Further, from the EIS results for Na||Na symmetric cells after 30 cycles operated at 1 mA cm^{-2}, the symmetric cells with S-3500 separator show a smaller charge-transfer resistance (R_{ct}) of 192.5 Ω than those with S-1000 (208.6 Ω) and GF/D (210.8 Ω) separators (see Figure S8, Supporting Information). This indicates the reduced resistance during Na^+ migration and relatively rapid charge-transfer kinetics with the S-3500 separator due to a favorably sodiophilic and highly aligned nanofibrous network. Besides, Na||Cu asymmetric cells with different separators were fabricated to assess the Na nucleation/deposition-stripping behavior using 1.0 M $NaClO_4$ in EC/DMC (1:1, v/v) solution. At a current density of 1 mA cm^{-2} and a cycling capacity of 2 mAh cm^{-2}, the Na||Cu cells with GF/D separator exhibit a very low CE of 34%, which is inferior to that of S-1000 (62%) and S-3500 (77%) separators at the second cycle (see Figure S9, Supporting Information). This could be ascribed to that carbonate-based electrolytes were unable to achieve a high reversibility of metallic Na stripping from the Cu substrate, unlike the existence of average CE of nearly 99.9% in ether-based electrolyte systems (e.g., diglyme),[73] but the S-3500 separator can enable the enhanced CE compared to other samples in the identical testing condition. Specifically, the Na||Cu cells with S-3500 separator show the lowest nucleation overpotential of only 2.2 mV than those of Na||Cu cells with S-1000 (11.8 mV) and GF/D (25.2 mV) separators, signifying the lowest interface resistance and improved Na-ion transport kinetics through the sodiophlic S-3500 separator.

To gain comprehensive insights into the functionalization and regulating/protection mechanism of this unique S-3500 separator, aligned microstructural analysis and electrochemical/mechanical simulations of the simulated Na electrodeposition process are employed to demonstrate its substantial benefits in suppressing Na dendritic growth. First, the 3D volume rendering of greyscales was employed via reconstructing the 2D "ortho-slices" tomograms stemming from X-ray computed microtomography. The subsequent "Xfiber" calculation was processed to visualize the presentative models, volume fraction, and orientation distribution of nanofibers in the S-1000 and S-3500 nanofibrous membranes, as displayed in **Figure 5**a–d and Figure S10, Supporting Information. The 3D reconstructions reveal that the relative randomly oriented or less-aligned nanofibers and several beads are observed in the as-formed S-1000 membrane (Figure 5b); meanwhile, the through-plane volume fractions undergo a surge fluctuation between 6 and 18% due to the structural randomness and instability (Figure S11, Supporting Information), verifying its noncontinuous, irregular and less-aligned microstructure. In sharp contrast, the as-spun S-3500 membrane comprises uniaxially aligned nanofibers (cylindric models, see Figure 5a) in the *x*-*y* plane via high-speed (3500 rpm) electrospinning and the volume fractions maintained at around 20–22% along the *z*-direction (see Figure S11, Supporting Information), presenting its micrometer-scale, continuous uniaxial alignment throughout the nanofibrous membranes with a higher structural homogeneity and integrity. The orientation distribution map is utilized to describe the orientation and content/intensity of all nanofibers at a spatial angle for quantitively defining the intensity ratio of nanofiber content, that is, alignment degree (Equations S7 and S8, Supporting Information).[74] The nanofibers of the S-3500 membrane manifest the maximum content (depicted as a dark red oval) along the longitudinal (±90°) direction and the minimum content (depicted as a dark blue oval) at the transverse (0°) direction in the *x*-*y* plane with a high calculated alignment degree (C_{max}/C_{min}) of 4.3 and a clear anisotropic orientation in S-3500 microstructures (Figure 5c and Figure S12, Supporting Information); nonetheless, a lower alignment degree of 2.1 is obtained for the as-spun S-1000 membranes, which reflects

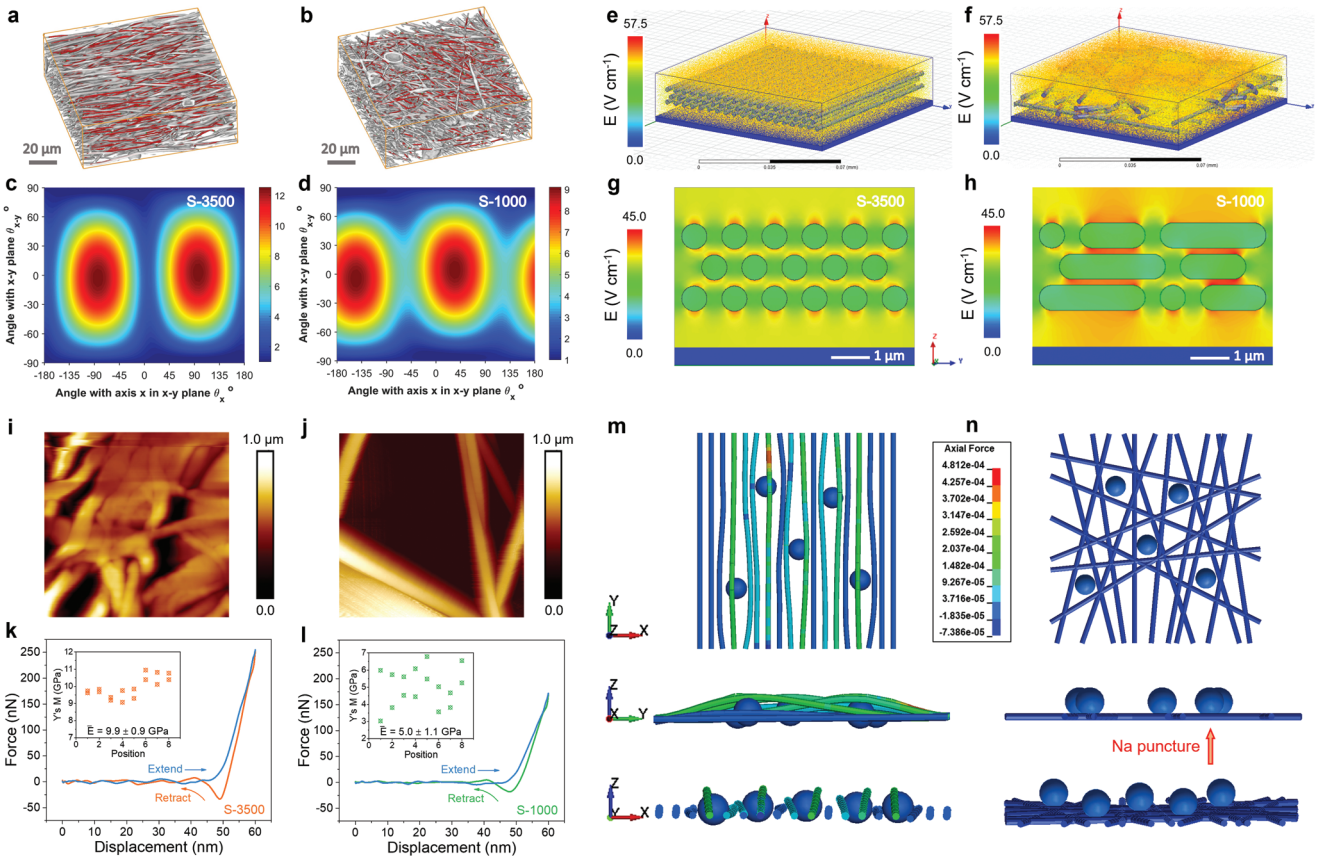

Figure 5. Theoretical simulations and mechanism analysis of CNC/PEI nanofibrous separators. a–d) 3D volume rendered images and an alignment distribution map of S-3500 (a,c) and S-1000 (b,d) nanofibrous membranes via Xfiber analysis from X-ray computed microtomography. e,f) 3D and g,h) 2D electric field distribution vector profiles of the Na-ions electrodeposition onto the metallic sodium with the S-3500 (e,g) and S-1000 (f,h) separators. i,j) AFM-based quantitative nanomechanics of S-3500 (i) and S-1000 (j) separators. Image area: 10 ×10 μm. k,l) Typical force–displacement curves of S-3500 (k) and S-1000 (l) separators. m,n) Von Mises stress distribution of the Na protrusion (denoted as blue balls) against the highly aligned S-3500 (m) and the randomly oriented S-1000 (n) nanofibrous separators.

insufficient and indistinct and more isotopic orientation in their microstructure (Figure 5d and Figure S12, Supporting Information).

Based on the as-extracted typical models of nanofibers, 2D and 3D finite element modeling was performed to simulate the electric field intensity distribution with two types of alignment-varying sodiophilic separators (i.e., S-3500 and S-1000) during the Na electrodeposition process (Figure 5e–h). In Figure 5f,h, the electric field intensity on the randomly oriented and layer-stacked scaffolds/skeletons from the S-1000 separator is obviously higher than that of the adjacent pores, allowing the accumulation of Na^+ flux at the concentrated nucleation sites and the growth of dendrites around the preferential protuberant tips, which could give rise to severely nonuniform Na deposition on the anode and eventually the internal short circuit of the cells.[75] On the contrary, with the shunting of layered and highly aligned frameworks/nanofibers in the S-3500 separators, the distribution of Na^+ flux becomes through-plane-oriented and increasingly uniform as the ions transport along the *Z*-axis; meanwhile, the sodiophilic groups from the CNC/PEI nanofibers help to trigger the concurrent and smooth Na deposition on the anode, in turn enabling a well-oriented and homogenous electric field due to its equipotential surface (see Figure 5e,g).[76] Accordingly, this unique highly aligned sodiophilic structure endows the S-3500 separator with self-regulating/orienting Na deposition and suppresses Na dendrite growth from a molecular level, accounting for the superior high-rate capability and cyclability of symmetric cells with the S-3500 separator.

Additionally, the mechanical properties at nano-scale of the S-1000 and S-3500 separators were investigated by atomic force microscopy (AFM) via quantitative nano-mechanics mode AFM (Figure 5i–l); the results are plotted as force (*F*) versus displacement (*d*) curves containing the extension and retraction process of the indenter based on Equation S9, Supporting Information. After imaging, a hard AFM silicon probe was used to put pressure onto the separators to simulate the puncture of a lithium dendrite, where the force applied to the probe was gradually increased. The plastic deformation is recognized to occur after elastic deformation when the extending curve and the retracting curve show a non-overlapping behavior called hysteresis.[77] According to Figure 5k,l, the S-1000 separator undergoes plastic deformation when the force was increased to 172 nN, whereas the S-3500 separator maintained elastic deformation when the applied force of probe is 255 nN. Notably, mapping of elastic modulus reveals that the highly aligned S-3500 separator

shows a higher value ≈9.9 ± 0.9 GPa (Figure 5k and Figure S13, Supporting Information) than 5.0 ± 1.1 GPa (Figure 5l) for the randomly oriented S-1000 separator; this suggests superior mechanical resistance enabled by the uniaxially aligned nanofibers and excellent puncture resistance capability to prevent sodium dendrites from piercing the separator.[78] Moreover, referring to the abovementioned elastic moduli and nanofiber diameter for the two types of CNC/PEI nanofibrous scaffolds, finite element modeling was carried out to further assist with evidencing the stress durability and distribution of S-1000 and S-3500 separators when moving blue balls toward the separators to imitate Na dendrite growth. It is notable that the von-Mises stress distribution demonstrates an effective mechanical tolerance or resistance in the highly aligned and compact S-3500 scaffolds (Figure 5m), in contrast to the randomly oriented S-1000 scaffolds with abundant defects or spaces which cannot avoid the growing Na dendrites (depicted as blue balls) puncturing through the S-1000 scaffold (Figure 5n), signifying the necessity of the highly oriented and closely packed structure. Therefore, the mechanical reliability of the S-3500 separator contributes to the beneficial long-term cycling stability via physically restraining Na dendrite puncture from a mechanical structural level to circumvent the short-circuit phenomenon.

To highlight the applicability of the S-3500 separator in practical Na-metal batteries, the electrochemical performance of Na||PTCDA cells with the S-3500 and reference GF/D separators was also investigated. The low-cost and environmental-friendly PTCDA was exploited as a new organic cathode material for SMBs on account of being one of the fundamental precursors in the dye industry, showing great potential to be used for the large-scale production of inexpensive and environmentally friendly SMBs;[79,80] the schematic structure of the organic PTCDA cathode and its corresponding working principle of this sodium–organic battery (i.e., Na||PTCDA cell) are sketched in **Figure 6**a. Notably, the unique S-3500 separator with uniaxially aligned and sodiophilic nanofibers/skeletons plays a dual role in being a highly oriented and chemical ion-redistributor to shunt the Na-ion flux and posing a mechanical barrier to physically block the puncture of Na dendrites for realizing stable, dendrite-less Na-metal batteries from a molecular and mechanical structural levels. Figure 6b,c reveals that the Na||PTCDA cell with the S-3500 separator reveals an increased rate capability compared to the GF/D separator. Specifically, the reversible capacities of the Na||PTCDA cell with the S-3500 separator are 125, 114, 107, 101, and 96 mAh g^{-1} (based on the weight of the cathode) at a current rate (C-rate) from 0.1 C to 2 C, higher than those of cells with a GF/D separator (108, 87, 71, 62 and 55 mAh g^{-1}). Moreover, the Na||PTCDA cell with a S-3500 separator demonstrates a remarkably stable cycling performance with a capacity retention of 63.2% and a CE of nearly 100% over 1000 cycles at 0.5 C, which surpasses those of Na||PTCDA cells with commercially available GF/D separators; they exhibit a severe and rapid capacity decay before the 400th cycle (see Figure 6d). Significantly, based on the active mass of both the anode and cathode, the Na||PTCDA cell with the S-3500 separator exhibits a high energy density of ≈256 Wh kg^{-1} and a high power density of ≈458 W kg^{-1}, which outperforms those of the Na||PTCDA cell with GF/D separator (≈190 Wh kg^{-1}, ≈386 W kg^{-1}) and other previously reported PTCDA-based Na-ion/-metal full battery configurations (see Table S4, Supporting Information).[69,81] Its sufficient energy output could power a green light-emitting diode (LED) as shown in Figure S14, Supporting Information.

To further evaluate the viability and practicality of the S-3500 separator materials, it is significant to compare the stack energy density normalized by the total mass of the entire stack including electrodes, electrolyte, and separator instead of the active mass of electrodes alone.[82] To this end, it is necessary to increase the mass loadings of the PTCDA cathode and reduce the thickness of the Na foil along with the thinner separator and the lean electrolyte to maximize the stack energy density. Therefore, the Na||PTCDA cell using a thinner Na foil (around 90 μm), a high-mass-loading PTCDA cathode (around 5.5 mg cm^{-2}), a thinner S-3500 separator (thickness: 24 μm, see Figure S15a, Supporting Information), and the lean amount of electrolyte (10 μL) was assembled. First, the cycling performance of Na||Na symmetric cells with the thinner S-3500 separator was tested at a current density of 1 mA cm^{-2} and the stripping/plating capacity of 0.5 mAh cm^{-2}, delivering a relatively stable voltage profile over 700 h (see Figure S15b, Supporting Information), which verifies the excellent cycling stability and good interfacial stability of the cell. Hence, the cell with thinner S-3500 separator can enable the tradeoff between the thickness of the separator and the stability of the electrochemical performance. Afterward, Figure S15c, Supporting Information shows the galvanostatic discharge-charge profiles of the abovementioned Na||PTCDA cells with the thinner S-3500 separator and the lean amount of electrolyte under different current densities, where the reversible capacities are 126, 117, 110, 97 and 91 mAh g^{-1} (based on the weight of the cathode). Accordingly, the employment of the thin S-3500 separator and the lean amount of electrolyte has no detrimental effect on the charge-discharge performance of Na||PTCDA cells, which also demonstrates the promise of deploying the thin S-3500 separator due to its excellent wettability (Figure S15d, Supporting Information).

Meanwhile, the stack energy densities of the Na||PTCDA cell with this specific configuration were calculated according to Equation S13, Supporting Information. The gravimetric stack energy density of 80 Wh kg^{-1} and the gravimetric stack power density of 344 W kg^{-1} are achieved in the Na||PTCDA cell with the thinner S-3500 separator. It is noteworthy that the stack energy densities of Na|thin S-3500|PTCDA cell make these batteries potentially competitive against other kinds of energy storage devices such as Cd-acid, Ni-Cd, and sodium-ion batteries (see Figure 6e),[10,83] which suggests its promise as low-cost and sustainable SMBs for practical applications in large-scale energy storage. With the adoption of an ultrathin Na foil (<25 μm), a high-mass-loading cathode (>10 mg cm^{-2}) and an afore-mentioned thin separator (around 20 μm), the stack energy density of the cell can be further enhanced in the future.

Synchronously, to probe the component of the SEI layer, ex situ X-ray photoelectron spectroscopy (XPS) investigations were performed with depth profiling to analyze the surface composition of the cycled Na-metal anode assembled with the S-3500 separator. In the high-resolution C 1s spectra (Figure 6f), the peaks located at ≈284.8, ≈286.5, ≈288.4 and ≈289.7 eV correspond to the C—C, C—O, C=O, and CO_3^{2-} groups, respectively, which involve typical reductive decomposition of the cyclic

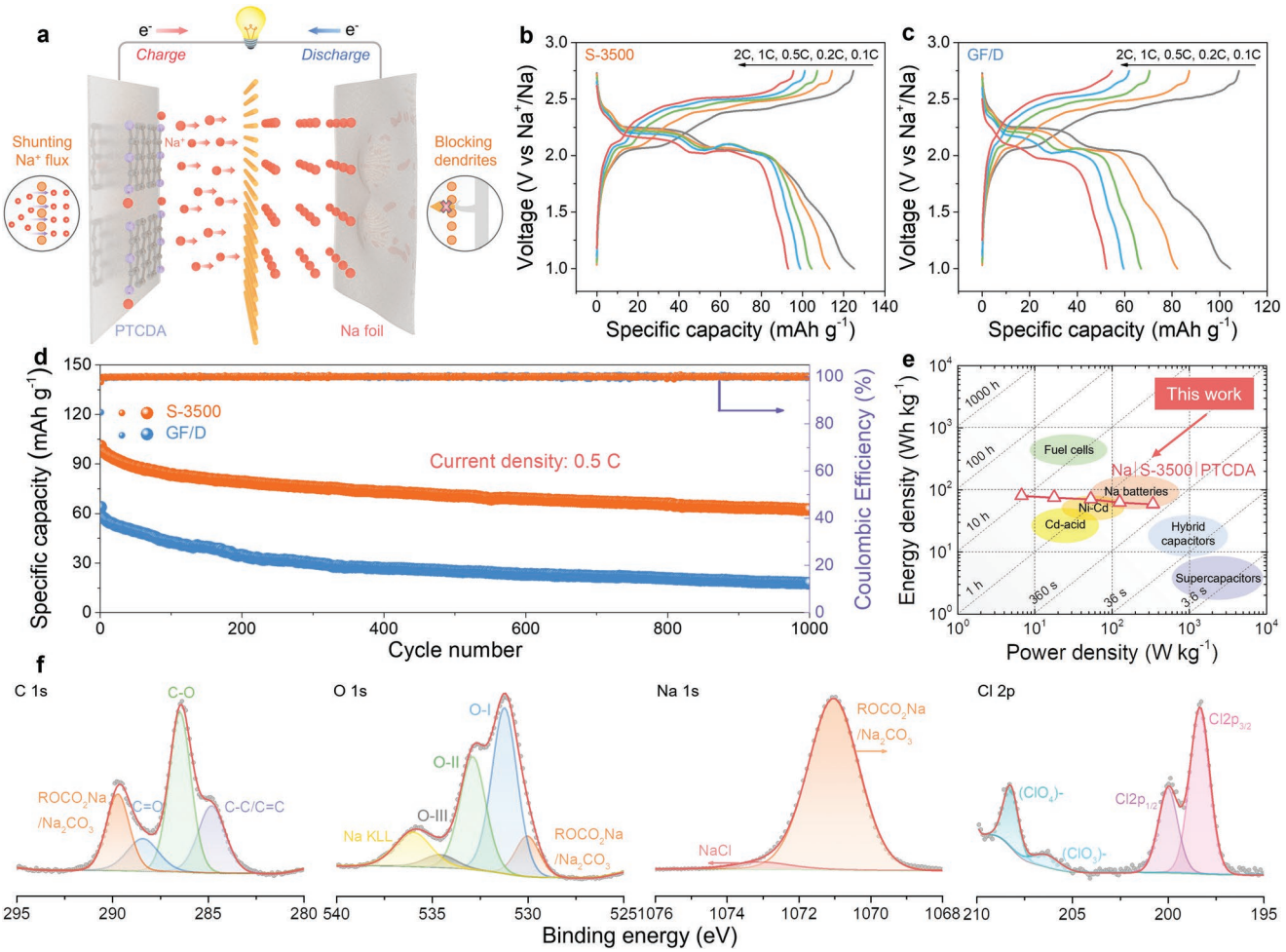

Figure 6. Electrochemical performances of Na||PTCDA cells with S-3500 and GF/D separators. a) Schematic working principle of the cell with the S-3500 separator. b,c) Galvanostatic discharge-charge profiles of Na||PTCDA cells with S-3500 (b) and GF/D (c) separators at various current densities (each curve represents the first cycle at the corresponding C-rate). d) Long-term cycling stability obtained at 0.5 C (1 C = 100 mA g^{-1}). e) Ragone plots of gravimetric stack energy density and gravimetric stack power density of the sodium–organic cell with the thin S-3500 separator in comparison with other kinds of energy-storage devices (the energy and power densities are normalized by the total mass of the entire stack including the anode, cathode, separator, and electrolyte). f) Ex situ XPS spectra of fitted C 1s, O 1s, Na 1s, and Cl 2p core levels for the cycled Na anode. (PTCDA: 3,4,9,10-perylene-tetracarboxylicacid-dianhydride).

carbonate electrolyte (1.0 M $NaClO_4$ in EC/DMC). Meanwhile, the analytical results from high-resolution O1s spectra demonstrate the components of C=O carbonyl groups (O-I), C-OH hydroxyl or C-O-C ether groups (O-II), O=C−OH carboxyl groups (O-III), Na KLL auger, and $ROCO_2Na/Na_2CO_3$ species appearing on the surface of the Na-metal anode.[84] From the high-solution Na 1s spectra, two peaks of sodium carbonates (Na_2CO_3) and sodium chloride (NaCl) could be detected at ≈1071.1 and ≈1073.1 eV, respectively. In the case of Cl 2p spectra, the binding energies of $Cl2p_{3/2}$ and $Cl2p_{1/2}$ are spotted at ≈198.3 and ≈199.9 eV, together with two deconvoluted peaks at ≈206.4 (ClO_3^-) and ≈208.2 (ClO_4^-).[85] Overall, the SEI layer formed in the sodiated carbonate electrolyte consists of the dominated organic species (≈64 at%) and partial inorganic components (i.e., $ROCO_2Na/Na_2CO_3$, NaCl, Na KLL auger, etc.) with an atomic content of ≈36 at% (Figure S16, Supporting Information), thus generating a continuous and stable phase with good flexibility,[10] which eliminates the SEI layer reconstruction and excessive electrolyte decomposition upon the consecutive plating/stripping process and eventually gives rise to the prolonged cyclability of the cell with S-3500 separator.[5]

3. Conclusions

We have proposed a novel, mechanically flexible, and multifunctional CNC/PEI nanofibrous separator (i.e., S-3500) with appealing physiochemical merits, such as excellent electrolyte wettability/affinity and ionic conductivity, definable porosity, optimum thickness, enhanced thermal resistance, and exceptional mechanical strength/modulus, via a simple and scalable electrospinning strategy by tailoring the rotational speed of a drum collector. Owing to the well-ordered arrays/nanofibers coupled abundant sodiophilic groups (e.g., C=O, −OH), the unique S-3500 separator endows an efficient and highly oriented route to self-regulating/aligning the Na-ion flux

distribution at a chemical molecule; meanwhile, its uniaxial highly aligned nanofibers with the tunable alignment degree allow physical suppression of the Na dendrite puncture at a mechanical structural level, which synergistically realized the stable, dendrite-less, and homogenous Na deposition behavior, as confirmed by both experimental and theoretical/simulation analysis. Benefiting from these advantages, the resulting symmetric Na‖Na cells with the S-3500 separators manifest remarkable and long-term Na cycling performances (i.e., ≥1000 h at 3 mA cm^{-2}, ≥700 h at 5 mA cm^{-2}). They also demonstrate outstanding rate capability up to 5 mA cm^{-2}, uniquely employed in low-cost carbonate electrolytes without any additional additives. In addition, the PTCDA‖Na cell with the S-3500 separator enables an ultralong cycle life (over 1000 cycles with 0.037% capacity fading per cycle), a superior energy density of ≈256 Wh kg^{-1} and power density of ≈458 W kg^{-1} over commercial GF/D separator in additive-free carbonate electrolyte.

The abovementioned results demonstrate a viable and practical strategy for constructing bifunctional, highly aligned ion-redistributors for homogenizing ion deposition for dendrite-arranged metal anodes, and serving as structural, mechanically flexible scaffolds to physically block dendrite growth. This approach provides a new perspective and design guideline to stabilize other metallic batteries such as potassium-, zinc-, aluminum-, calcium- and magnesium-metal-based systems, exhibiting a promising solution for enhancing their cyclability combined with the optimized electrolyte systems. Considering the renewability of the precursor and the scalability at relatively low cost (e.g., separator, electrolyte, and cathode) in this environmentally benign synthesis process, this work offers new opportunities for realizing low-cost, sustainable, safe-credible, and high-energy-density rechargeable Na-metal batteries in large-scale energy storage in the near future.

4. Experimental Section

Fabrication of Random/Aligned Nanofibrous Separators: First, freeze-dried CNCs were obtained from *Laminaria hyperborea* seaweed cellulose via an acid-hydrolysis approach.[44,86] In a typical synthesis procedure, 5.12 g of PEI (ULTEM 1000) was dissolved in 20 mL of 1-methyl-2-pyrrolidone (NMP) by magnetic stirring at room temperature for 12 h, followed by dispersing 5 wt% of CNCs (based on the weight of PEI) in the above mixture under tip sonication at 15% to obtain a homogenous solution. Then, the resulting spinning solution was pumped at a flow rate of 1.0 mL h^{-1} through a stainless-steel syringe needle connected to a high-voltage power supply carrying a DC voltage of 20 kV. The tip-to-collector distance was set at ≈20 cm and the nanofibers were directly collected on a grounded piece of aluminum foil attached to a rotating drum collector using a speed controller with rotational speed ranging from 0 to 4000 rpm. After setting the rotational speed of 3500 rpm (i.e., technically maximum speed), the as-prepared aligned nanofibrous membranes were dried at 80 °C overnight and carefully peeled off from the aluminum foil; these samples were designated as S-3500. For comparison, the nanofibrous membranes with randomly oriented nanofibers (denoted as S-1000) were also fabricated at a relatively low rotational speed of 1000 rpm, while other steps were kept the same as the S-3500 sample. The S-1000 and S3500 samples were cut into circular separators (16 mm in diameter) with areal weights (A_W) of 34.4 ± 0.03 g m^{-2} and 39.4 ± 0.02 g m^{-2}, respectively (Equation S1, Supporting Information). For comparison, commercial Celgard-2500 (monolayer PP, Cambridge Energy Solutions; called generically "Celgard") and glass microfiber filters membrane (Grade GF/D, Whatman) were also investigated for the evaluation of their properties and performances.

Materials Characterizations: The morphology and orientation of the CNC/PEI nanofibrous membranes were investigated by SEM (JEOL IT300) and X-ray microtomography (Versa 620, Zeiss) with accelerating voltages of 15 and 80 kV, respectively. TEM (JEOL 1400) was performed to observe the morphology and structure of the prepared CNCs by depositing an aqueous suspension of the CNC on carbon film-coated copper grids, and negatively staining using uranyl acetate. A contact angle goniometer (DSA25S, Kruss) was applied to determine the surface wettability of the separators with the 1.0 M $NaClO_4$ in 1:1 (v/v) ethylene carbonate/dimethyl carbonate (EC/DMC). FT-IR spectra of CNC/PEI composite separators were acquired using an FT-IR spectrometer (Spectrum Two, PerkinElmer) operating under attenuated total reflectance (ATR). The pore size distributions were determined by using N_2 adsorption/desorption apparatus (TriStar II PLUS, Micromeritics) via the non-local density-functional-theory (NLDFT) method. Thermogravimetric analysis TGA was performed using a Netzsch STA 449 F3 thermal analyzer from 30 to 1300 °C at a heating rate of 10 K min^{-1} under a nitrogen environment (50 mL min^{-1}). Tensile tests were conducted using a tensile stage controller (DEBEN) with a 10 N load cell at a crosshead speed of 0.5 mm min^{-1}. Elastic moduli of the separators were measured using AFM (Bruker Dimension Icon with ScanAsyst) in peak force quantitative nanomechanics (QNM) mode and analyzed by Nanoscope Analysis software. PeakForce tapping mode was adopted in AFM imaging using a SCOUT-350 RAI (Nunano) silicon probe with Al reflective coating (spring constant: 42 N m^{-1}). Before measurements, the probe was calibrated by using a standard highly oriented pyrolytic graphite (HOPG, modulus ≈ 18 GPa) sample in an Ar-filled glove box for good precision. Force curves of the samples were obtained by force spectroscopy mode with typical scanning rate of 1 Hz and a loading force of 300 nN. The moduli of the separators were estimated based on data collected at various positions and on at least three different samples. For the ex situ SEM observations of the cycled anode and separator sides, the cells with GF/D, S-1000 and S-3500 separators were plated/stripped for 30 cycles at a current density of 1 mA cm^{-2} with a stripping/plating capacity of 0.5 mAh cm^{-2}. The post-tested sodium symmetric cells were disassembled in an argon-filled glove box, and then the sodium-metal anode was cleaned in DMC solution. The dried sodium-metal anode was subsequently sealed in a vacuum transferring capsule to prevent exposure to air for employing ex situ X-ray photoelectron spectroscopy (XPS) measurements, using, K-Alpha (Thermo Fisher) XPS equipped with monochromatic Al-Kα as the excitation source. The binding energy was calibrated based on the C_{1s} peak at 284.8 eV.

Electrochemical Measurements: All the cells were assembled with MTI CR2032 coin-type cells in an Argon-filled glovebox (H_2O < 0.5 ppm; O_2 < 0.5 ppm, MBRAUN). The electrolytes (100 µL for S-1000 and S-3500; 200 µL for GF/D) used for both Na‖Na symmetric cells, Na‖Cu asymmetric cells, and Na‖PTCDA cells were 1.0 M $NaClO_4$ in a mixture of EC/DMC (1:1 by volume) without any other electrolyte additives. Electrochemical impedance spectroscopy (EIS) measurements were collected with symmetric stainless steel‖stainless steel cells over a frequency range of 0.01 to 10^5 Hz using an Autolab PGSTAT204 electrochemical workstation. The Na‖Na symmetric cells were assembled with two Na foils (thickness: ≈100 µm) as the working electrode and reference electrode, respectively, and GF/D (Whatman), S-1000, or S-3500 separators as the separators. The Na‖Cu asymmetric cells were prepared with Na foil (thickness: ≈100 µm) as the counter/reference electrode, Cu foil as the working electrode, and the GF/D or S-3500 membranes as the separator. Afterward, the PTCDA cathode was prepared by mixing 3,4,9,10-perylene-tetracarboxylicacid-dianhydride (PTCDA), carbon black, and polyvinylidene fluoride (PVDF) at a weight ratio of 6:2:2 in NMP and then pasting on an aluminum foil. The Na ‖ PTCDA cells consisting of a PTCDA cathode (mass loading of ≈2.0 mg cm^{-2}), Na foil, and GF/D or S-3500 separators were measured between 1.00 , N 2.75 V at a varying C-rate. Pre-cycling of the Na‖ PTCDA cells

were performed in the potential window between 1.00 and 2.75 V at a rate of C/20 at room temperature, for the benefit of pre-forming a stable SEI film on the electrode surfaces to minimize the irreversible effect in the initial discharge process.

Imaging Analysis and Theoretical Simulations: The reconstructed 3D volume of nanofibrous membranes (i.e., S-1000 and S-3500) was imported into the commercial software package Avizo (2019.1, Thermo Fisher Scientific) for microstructural characterization and post-modeling via greyscales derived from X-ray computed microtomography data. To de-noise and smooth the data, a 3D Median filter (iterations = 3) and interactive thresholding (intensity range: 85–255) were applied. The orientation distributions were mapped by tomogram segmentation in a cube of 600 × 600 × 200 voxels (voxel size: 0.2 µm) via cylinder correlation in Xfiber extension. The volume fractions were calculated in Avizo software, and all other computational analysis was performed on Matlab software (2021.b) on binarized volumetric images processed as previously mentioned. Finite element modeling conducted by Ansys Maxwell software, adapted to simulate the electric field distribution with a sodiophilic separator (S-3500 and S-1000) during Na electrodeposition. The S-3500 separator was modeled as three layers of highly aligned cylinder bundles with an aperture of 0.55 µm and a cylinder spacing of 0.34 µm. An overpotential of 0.1 V was employed between the anode and electrolyte sides, and the boundary of finite elements was chosen as Bollon type during the simulation. The electrical conductivity of metallic sodium was set to 2.1×10^7 S m^{-1} and the ionic conductivity of 1 M $NaClO_4$ in 1:1 EC/DMC electrolyte was 2.1×10^7 and 1.0 S m^{-1}, respectively. For the von Mises stress distribution modeling, the model (3D shell) was built with LS-DYNA finite element software. To simplify the models, blue balls (diameter of 5µm) representing Na protrusion were applied onto two types of CNC/PEI nanofibrous scaffold with a length of 50 µm and a width of 1 µm at a constant force of 0.01 N. The elastic modulus of S-1000 and S-3500 was set to be 5.0 and 9.9 GPa, respectively.

Supporting Information

Supporting Information is available from the Wiley Online Library or from the author.

Acknowledgements

J.W. and Z.X. contributed equally to this work. This work was supported by a grant from the Engineering and Physical Sciences Research Council (EP/V002651/1). The authors would like to thank Dr. Mark Dorris at the Edinburgh Napier University for providing the freeze-dried CNCs. The authors appreciate the assistance from Dr. Byung Chul Kim and Dr. Xiaochuan Sun for offering the license and guidance about LS-DYNA software. The authors also would like to thank Prof. Ian Hamerton for the supply of commercial polyetherimide and Suihua He for the training regarding TGA. J.W. and X.S. acknowledge the China Scholarship Council for the Ph.D. scholarships.

Conflict of Interest

The authors declare no conflict of interest.

Data Availability Statement

The data that support the findings of this study are available from the corresponding author upon reasonable request.

Keywords

carbonate electrolytes, highly aligned nanofibers, long cycle life, sodium-metal batteries, sustainable separators

Received: July 13, 2022
Revised: September 12, 2022
Published online: October 26, 2022

[1] S. Qiu, L. Xiao, M. L. Sushko, K. S. Han, Y. Shao, M. Yan, X. Liang, L. Mai, J. Feng, Y. Cao, *Adv. Energy Mater.* **2017**, *7*, 1700403.
[2] A. Devaraj, M. Gu, R. Colby, P. Yan, C. M. Wang, J. Zheng, J. Xiao, A. Genc, J. Zhang, I. Belharouak, *Nat. Commun.* **2015**, *6*, 8014.
[3] Y. Fu, Q. Wei, G. Zhang, S. Sun, *Adv. Energy Mater.* **2018**, *8*, 1703058.
[4] D. Kundu, E. Talaie, V. Duffort, L. F. Nazar, *Angew. Chem., Int. Ed.* **2015**, *54*, 3431.
[5] J. Wang, Z. Xu, J. C. Eloi, M. M. Titirici, S. J. Eichhorn, *Adv. Funct. Mater.* **2022**, *32*, 2110862.
[6] Y. Zhao, L. V. Goncharova, A. Lushington, Q. Sun, H. Yadegari, B. Wang, W. Xiao, R. Li, X. Sun, *Adv. Mater.* **2017**, *29*, 1606663.
[7] F. Heredia, A. L. Martinez, V. Surraco Urtubey, *J. Energy Nat. Resour. Law* **2020**, *38*, 213.
[8] B. Sun, P. Xiong, U. Maitra, D. Langsdorf, K. Yan, C. Wang, J. Janek, D. Schröder, G. Wang, *Adv. Mater.* **2020**, *32*, 1903891.
[9] Z. Xu, J. Wang, Z. Guo, F. Xie, H. Liu, H. Yadegari, M. Tebyetekerwa, M. P. Ryan, Y.-S. Hu, M.-M. Titirici, *Adv. Energy Mater.* **2022**, *12*, 2200208.
[10] Z. Xu, Z. Guo, R. Madhu, F. Xie, R. Chen, J. Wang, M. Tebyetekerwa, Y.-S. Hu, M.-M. Titirici, *Energy Environ. Sci.* **2021**, *14*, 6381.
[11] C. Xia, R. Black, R. Fernandes, B. Adams, L. F. Nazar, *Nat. Chem.* **2015**, *7*, 496.
[12] X. Hu, J. Sun, Z. Li, Q. Zhao, C. Chen, J. Chen, *Angew. Chem., Int. Ed.* **2016**, *55*, 6482.
[13] X. Liu, W. Ma, X. Lei, S. Zhang, Y. Ding, *Adv. Funct. Mater.* **2020**, *30*, 2002120.
[14] S. Wei, S. Xu, A. Agrawral, S. Choudhury, Y. Lu, Z. Tu, L. Ma, L. A. Archer, *Nat. Commun.* **2016**, *7*, 11722.
[15] B. R. Kim, G. Jeong, A. Kim, Y. Kim, M. G. Kim, H. Kim, Y. J. Kim, *Adv. Energy Mater.* **2016**, *6*, 1600862.
[16] X. Mu, H. Pan, P. He, H. Zhou, *Adv. Mater.* **2020**, *32*, 1903790.
[17] H. Yadegari, Y. Li, M. N. Banis, X. Li, B. Wang, Q. Sun, R. Li, T.-K. Sham, X. Cui, X. Sun, *Energy Environ. Sci.* **2014**, *7*, 3747.
[18] L. Ma, J. Cui, S. Yao, X. Liu, Y. Luo, X. Shen, J.-K. Kim, *Energy Storage Mater.* **2020**, *27*, 522.
[19] H. Wang, E. Matios, J. Luo, W. Li, *Chem. Soc. Rev.* **2020**, *49*, 3783.
[20] X. Chen, X. Shen, B. Li, H. J. Peng, X. B. Cheng, B. Q. Li, X. Q. Zhang, J. Q. Huang, Q. Zhang, *Angew. Chem., Int. Ed.* **2018**, *57*, 734.
[21] B. Lee, E. Paek, D. Mitlin, S. W. Lee, *Chem. Rev.* **2019**, *119*, 5416.
[22] J. Lee, Y. Lee, J. Lee, S.-M. Lee, J.-H. Choi, H. Kim, M.-S. Kwon, K. Kang, K. T. Lee, N.-S. Choi, *ACS Appl. Mater. Interfaces* **2017**, *9*, 3723.
[23] Y. Lee, J. Lee, J. Lee, K. Kim, A. Cha, S. Kang, T. Wi, S. J. Kang, H.-W. Lee, N.-S. Choi, *ACS Appl. Mater. Interfaces* **2018**, *10*, 15270.
[24] S. Choudhury, S. Wei, Y. Ozhabes, D. Gunceler, M. J. Zachman, Z. Tu, J. H. Shin, P. Nath, A. Agrawal, L. F. Kourkoutis, *Nat. Commun.* **2017**, *8*, 898.
[25] H. Wang, C. Wang, E. Matios, W. Li, *Nano Lett.* **2017**, *17*, 6808.
[26] Y. Zhao, K. R. Adair, X. Sun, *Energy Environ. Sci.* **2018**, *11*, 2673.
[27] H. Gao, S. Xin, L. Xue, J. B. Goodenough, *Chem* **2018**, *4*, 833.
[28] C. Luo, T. Shen, H. Ji, D. Huang, J. Liu, B. Ke, Y. Wu, Y. Chen, C. Yan, *Small* **2020**, *16*, 1906208.

[29] S. Liu, S. Tang, X. Zhang, A. Wang, Q.-H. Yang, J. Luo, *Nano Lett.* **2017**, *17*, 5862.
[30] B. Sun, P. Li, J. Zhang, D. Wang, P. Munroe, C. Wang, P. H. Notten, G. Wang, *Adv. Mater.* **2018**, *30*, 1801334.
[31] A. Wang, X. Hu, H. Tang, C. Zhang, S. Liu, Y. W. Yang, Q. H. Yang, J. Luo, *Angew. Chem., Int. Ed.* **2017**, *129*, 12083.
[32] H. Tian, Z. W. Seh, K. Yan, Z. Fu, P. Tang, Y. Lu, R. Zhang, D. Legut, Y. Cui, Q. Zhang, *Adv. Energy Mater.* **2017**, *7*, 1602528.
[33] D. Lei, Y.-B. He, H. Huang, Y. Yuan, G. Zhong, Q. Zhao, X. Hao, D. Zhang, C. Lai, S. Zhang, *Nat. Commun.* **2019**, *10*, 4244.
[34] C. Zhou, J. Wang, X. Zhu, K. Chen, Y. Ouyang, Y. Wu, Y.-E. Miao, T. Liu, *Nano Res.* **2021**, *14*, 1541.
[35] H. Lee, M. Yanilmaz, O. Toprakci, K. Fu, X. Zhang, *Energy Environ. Sci.* **2014**, *7*, 3857.
[36] Q. Zhao, S. Stalin, C.-Z. Zhao, L. A. Archer, *Nat. Rev. Mater.* **2020**, *5*, 229.
[37] Z. Li, K. Zhu, P. Liu, L. Jiao, *Adv. Energy Mater.* **2021**, 2100359.
[38] J. Qin, H. Shi, K. Huang, P. Lu, P. Wen, F. Xing, B. Yang, M. Ye, Y. Yu, Z.-S. Wu, *Nat. Commun.* **2021**, *12*, 5786.
[39] M. Zhu, G. Wang, X. Liu, B. Guo, G. Xu, Z. Huang, M. Wu, H. K. Liu, S. X. Dou, C. Wu, *Angew. Chem., Int. Ed.* **2020**, *132*, 6658.
[40] H. Hao, T. Hutter, B. L. Boyce, J. Watt, P. Liu, D. Mitlin, *Chem. Rev.* **2022**, *122*, 8053.
[41] Y. Wang, Y. Wang, Y.-X. Wang, X. Feng, W. Chen, X. Ai, H. Yang, Y. Cao, *Chem* **2019**, *5*, 2547.
[42] S. J. Eichhorn, *Soft Matter* **2011**, *7*, 303.
[43] S. J. Eichhorn, A. Etale, J. Wang, L. A. Berglund, Y. Li, Y. Cai, C. Chen, E. D. Cranston, M. A. Johns, Z. Fang, G. Li, L. Hu, M. Khandelwal, K. Y. Lee, K. Oksman, S. Pinitsoontorn, F. Quero, A. Sebastian, M. M. Titirici, Z. Xu, S. Vignolini, B. Frka-Petesic, *J. Mater. Sci.* **2022**, *57*, 5697.
[44] A. J. Onyianta, D. O'Rourke, D. Sun, C.-M. Popescu, M. Dorris, *Cellulose* **2020**, *27*, 7997.
[45] Y. Wang, H. Dong, N. Katyal, H. Hao, P. Liu, H. Celio, G. Henkelman, J. Watt, D. Mitlin, *Adv. Mater.* **2022**, *34*, 2106005.
[46] D. Li, Y. Wang, Y. Xia, *Adv. Mater.* **2004**, *16*, 361.
[47] Y. Liu, X. Zhang, Y. Xia, H. Yang, *Adv. Mater.* **2010**, *22*, 2454.
[48] B. Li, S. Pan, H. Yuan, Y. Zhang, *Composites, Part A* **2016**, *90*, 380.
[49] C. Li, S. Liu, C. Shi, G. Liang, Z. Lu, R. Fu, D. Wu, *Nat. Commun.* **2019**, *10*, 1363.
[50] H. Liao, Y. Wu, M. Wu, X. Zhan, H. Liu, *Cellulose* **2012**, *19*, 111.
[51] H.-J. Lee, J.-M. Lim, H.-W. Kim, S.-H. Jeong, S.-W. Eom, Y. T. Hong, S.-Y. Lee, *J. Membr. Sci.* **2016**, *499*, 526.
[52] P. J. Kim, V. G. Pol, *Adv. Energy Mater.* **2018**, *8*, 1802665.
[53] J. Xiao, *Science* **2019**, *366*, 426.
[54] K. Lee, Y. J. Lee, M. J. Lee, J. Han, J. Lim, K. Ryu, H. Yoon, B. H. Kim, B. J. Kim, S. W. Lee, *Adv. Mater.* **2022**, *34*, 2109767.
[55] C. F. Francis, I. L. Kyratzis, A. S. Best, *Adv. Mater.* **2020**, *32*, 1904205.
[56] X. Feng, M. Ouyang, X. Liu, L. Lu, Y. Xia, X. He, *Energy Storage Mater.* **2018**, *10*, 246.
[57] P. Balakrishnan, R. Ramesh, T. P. Kumar, *J. Power Sources* **2006**, *155*, 401.
[58] J. Golebiewski, A. Galeski, *Compos. Sci. Technol.* **2007**, *67*, 3442.
[59] K. Xu, Y. Qin, T. Xu, X. Xie, J. Deng, J. Qi, C. Huang, *J. Membr. Sci.* **2019**, *592*, 117364.
[60] Q. Liu, Y. Liu, X. Jiao, Z. Song, M. Sadd, X. Xu, A. Matic, S. Xiong, J. Song, *Energy Storage Mater.* **2019**, *23*, 105.
[61] A. M. Barbe, P. A. Hogan, R. A. Johnson, *J. Membr. Sci.* **2000**, *172*, 149.
[62] S. S. Chi, X. G. Qi, Y. S. Hu, L. Z. Fan, *Adv. Energy Mater.* **2018**, *8*, 1702764.
[63] S.-H. Park, P. J. King, R. Tian, C. S. Boland, J. Coelho, C. Zhang, P. McBean, N. McEvoy, M. P. Kremer, D. Daly, J. N. Coleman, V. Nicolosi, *Nat. Energy* **2019**, *4*, 560.
[64] M. Guo, H. Dou, W. Zhao, X. Zhao, B. Wan, J. Wang, Y. Yan, X. Wang, Z.-F. Ma, X. Yang, *Nano Energy* **2020**, *70*, 104479.
[65] W. Liu, Z. Chen, Z. Zhang, P. Jiang, Y. Chen, E. Paek, Y. Wang, D. Mitlin, *Energy Environ. Sci.* **2021**, *14*, 382.
[66] H. Wang, Y. Wu, Y. Wang, T. Xu, D. Kong, Y. Jiang, D. Wu, Y. Tang, X. Li, C.-S. Lee, *Nano-Micro Lett.* **2022**, *14*, 23.
[67] C. Wang, H. Wang, E. Matios, X. Hu, W. Li, *Adv. Funct. Mater.* **2018**, *28*, 1802282.
[68] W. Luo, Y. Zhang, S. Xu, J. Dai, E. Hitz, Y. Li, C. Yang, C. Chen, B. Liu, L. Hu, *Nano Lett.* **2017**, *17*, 3792.
[69] H. Yang, F. He, M. Li, F. Huang, Z. Chen, P. Shi, F. Liu, Y. Jiang, L. He, M. Gu, *Adv. Mater.* **2021**, *33*, 2106353.
[70] L. Ma, M. A. Schroeder, O. Borodin, T. P. Pollard, M. S. Ding, C. Wang, K. Xu, *Nat. Energy* **2020**, *5*, 743.
[71] C. Wei, L. Tan, Y. Zhang, H. Jiang, B. Xi, S. Xiong, J. Feng, *J. Mater. Sci. Technol.* **2022**, *48*, 447.
[72] W. Luo, C. F. Lin, O. Zhao, M. Noked, Y. Zhang, G. W. Rubloff, L. Hu, *Adv. Energy Mater.* **2017**, *7*, 1601526.
[73] Z. W. Seh, J. Sun, Y. Sun, Y. Cui, *ACS Cent. Sci.* **2015**, *1*, 449.
[74] Q. Zhang, W. Lu, F. Scarpa, D. Barton, K. Rankin, Y. Zhu, Z.-Q. Lang, H.-X. Peng, *Mater. Des.* **2021**, *211*, 110139.
[75] L. Wang, J. Shang, Q. Huang, H. Hu, Y. Zhang, C. Xie, Y. Luo, Y. Gao, H. Wang, Z. Zheng, *Adv. Mater.* **2021**, *33*, 2102802.
[76] X. Liu, N. Xie, J. Xue, M. Li, C. Zheng, J. Zhang, Y. Qin, Y. Yin, D. R. Dekel, M. D. Guiver, *Nat. Energy* **2022**, *7*, 329.
[77] D. Guo, D. B. Shinde, W. Shin, E. Abou-Hamad, A.-H. Emwas, Z. Lai, A. Manthiram, *Adv. Mater.* **2022**, *34*, 2201410.
[78] C. Yan, X. B. Cheng, Y. X. Yao, X. Shen, B. Q. Li, W. J. Li, R. Zhang, J. Q. Huang, H. Li, Q. Zhang, *Adv. Mater.* **2018**, *30*, 1804461.
[79] W. Luo, M. Allen, V. Raju, X. Ji, *Adv. Energy Mater.* **2014**, *4*, 1400554.
[80] F. Jing, T. Huang, G. Tao, L. Ma, D. Lu, R. Liu, X. Xi, D. Wu, *Electrochim. Acta* **2018**, *276*, 207.
[81] G. Zhou, Y. E. Miao, Z. Wei, L. Mo, F. Lai, Y. Wu, J. Ma, T. Liu, *Adv. Funct. Mater.* **2018**, *28*, 1804629.
[82] Y. Gogotsi, P. Simon, *Science* **2011**, *334*, 917.
[83] Z. Xu, J. Wang, *Adv. Energy Mater.* **2022**, *12*, 2201692.
[84] Y. Jiang, Y. Yang, F. Ling, G. Lu, F. Huang, X. Tao, S. Wu, X. Cheng, F. Liu, D. Li, *Adv. Mater.* **2022**, *34*, 2109439.
[85] J. Song, G. Jeong, A.-J. Lee, J. H. Park, H. Kim, Y.-J. Kim, *ACS Appl. Mater. Interfaces* **2015**, *7*, 27206.
[86] J. Wang, T. R. Pozegic, Z. Xu, R. Nigmatullin, R. L. Harniman, S. J. Eichhorn, *Compos. Sci. Technol.* **2019**, *182*, 107744.